Applied Surface Science 542 (2021) 148660

Contents lists available at ScienceDirect

Applied Surface Science

journal homepage: www.elsevier.com/locate/apsusc

Full Length Article

Plasmon-exciton coupling in dielectric-metal hybrid nanocavities with an embedded two-dimensional material

Hongxin Huang, Fu Deng, Jin Xiang, Shulei Li, Sheng Lan *

Guangdong Provincial Key Laboratory of Nanophotonic Functional Materials and Devices, School of Information and Optoelectronic Science and Engineering, South China Normal University, Guangzhou 510006, China

ARTICLE INFO

Keywords:
Plasmon
Exciton
Silicon nanoparticle
Gold film
Two-dimensional material
Strong coupling

ABSTRACT

The interaction between light and matter has long been the research topic in many scientific disciplines. So far, strong plasmon-exciton coupling has been demonstrated in a variety of plasmonic nanocavities with embedded two-dimensional materials. Here, we proposed a hybrid nanocavity, which is composed of a silicon (Si) nanoparticle and a thin gold (Au) film, to realize strong plasmon-exciton coupling with an embedded two-dimensional material (WS_2 monolayer). It was found that the optical resonances of the hybrid nanocavity originate mainly from the coherent interactions of the Mie resonances supported by the Si nanoparticle and their mirror images induced by the Au film. Their optical properties, including electric field enhancements and damping rates, depend strongly on the excitation scheme of the nanocavity. It was revealed numerically and demonstrated experimentally that strong plasmon-exciton coupling can only be achieved by exploiting the optical mode formed by the interference of the electric dipole and its mirror image when the nanocavity is excited from the Au film side. Our findings pave the way for realizing strong plasmon-exciton coupling in dielectric-metal hybrid nanocavities and open new horizons for designing novel photonic devices in which the light-matter interaction can be manipulated.

1. Introduction

The interaction between light and matter is essential to many contemporary scientific disciplines, especially in the field of resonance coupling. Resonance coupling is a phenomenon that happens when an optical resonator interacts with a quantum emitter. It is of great importance not only for fundamental research but also for the practical applications in nanophotonics, such as exciton polarization laser [1], all-optical switch [2] and quantum information processing [3]. In the weak coupling regime, the radiation efficiency of emitters can be manipulated by the so-called Purcell effect [4–9]. However, strong coupling occurs when the energy exchange between light and emitters exceeds any of their intrinsic dissipation rates. In this case, an energy splitting, i.e., Rabi splitting [10], is usually observed in the spectrum of scattering or luminescence. So far, strong coupling has been demonstrated in many systems, such as optical micro-cavities with high quality factors [11–14] and plasmonic nanostructures with large electric field enhancement factors and small mode volumes [15–29].

Apparently, there are two ways towards the realization of strong plasmon-exciton coupling. One is to enhance the coupling strength between plasmons and excitons and the other is to reduce the damping rate of the plasmonic nanocavity. Although organic molecules and quantum dots can interact strongly with plasmonic nanocavities to realize strong and even super coupling [15–19], a large number of organic molecules or quantum dots is required because they interact with the optical modes in disordered ways. Moreover, organic molecules and quantum dots suffer from oxidation and photo-bleaching, which undoubtedly limit their applications in nanoscale photonic devices.

Transition metal dichalcogenides (TMDCs), which can be described by chemical formula MX_2 (M is Mo/W; X is S/Se) are semiconductor materials with band gap energies spanning the visible light to near infrared spectral range. They have attracted great interest in the fields of optoelectronics and photonics [30–33]. Owing to their large dipole moment and optical stability, TMDCs have been widely employed in the investigation of strong light-matter interaction. For example, the coupling between the surface plasmon resonances (SPRs) excited in silver (Ag) nanorods and the excitons in WSe_2 monolayer was investigated [20]. By increasing the thickness of the coverage of an Ag nanorod, an anti-crossing behavior was observed through the shift of the SPR of the Ag nanorod. Unfortunately, the energy splitting did not meet the

* Corresponding author.
E-mail address: slan@scnu.edu.cn (S. Lan).

https://doi.org/10.1016/j.apsusc.2020.148660
Received 27 August 2020; Received in revised form 13 November 2020; Accepted 29 November 2020
Available online 3 December 2020

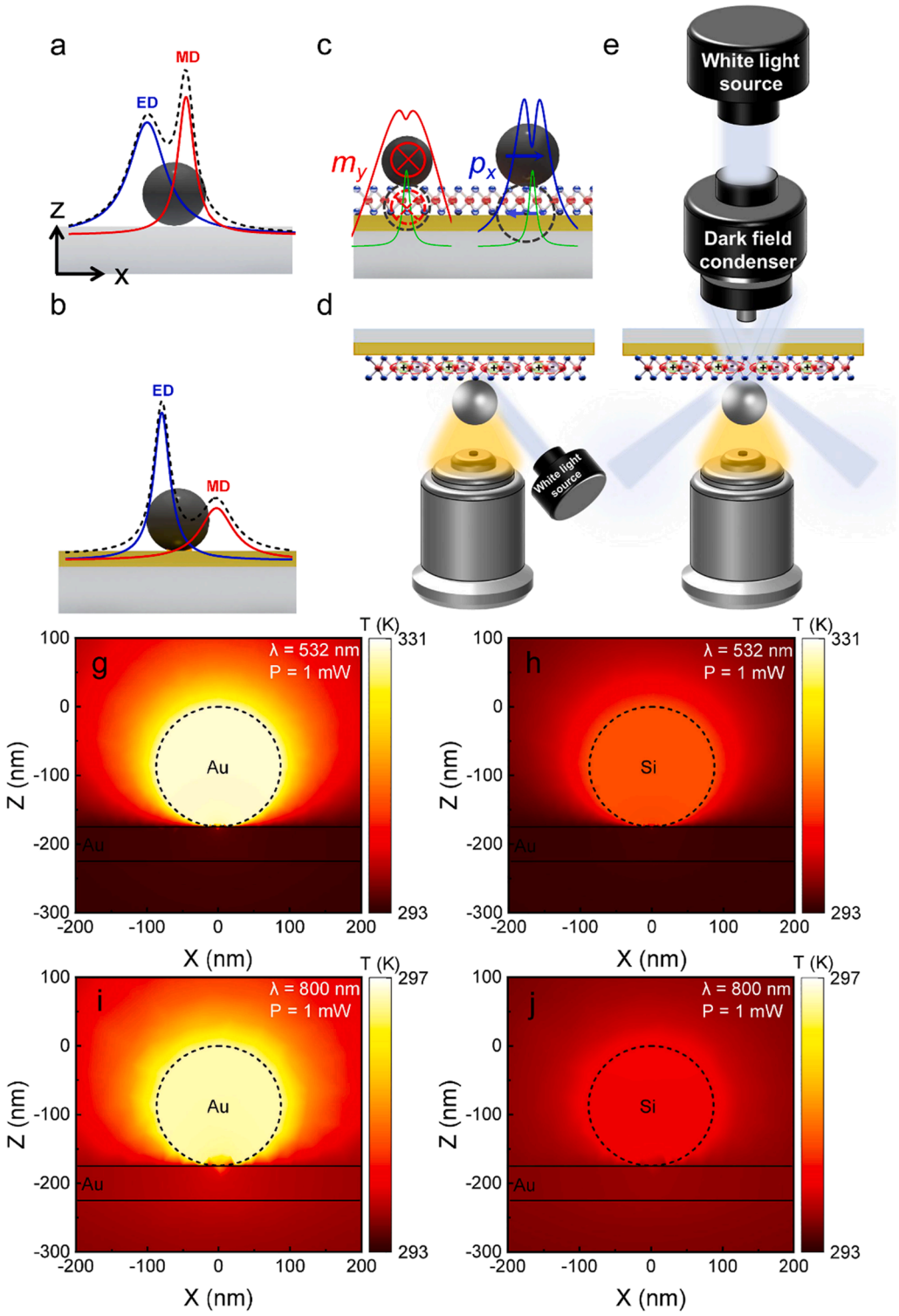

Fig. 1. (a) Scattering spectrum calculated for a Si nanoparticle placed on a SiO_2 substrate (dashed curve), which is composed of the contributions of ED (blue curve) and MD (red curve). (b) Scattering spectrum calculated for a Si nanoparticle placed on an Au/SiO_2 substrate (dashed curve). In this case, the coherent interaction of the ED (p_x) and its mirror-image (p_{xm}) leads to a narrowed resonance (blue curve) while the coherent interaction of the MD (m_y) and its mirror-image (m_{ym}) leads to a broadened resonance (red curve). (c) Coupling of the m_y-m_{ym} mode in a small Si nanoparticle placed on an Au/SiO_2 substrate with the excitons in a WS_2 monolayer (red curve). Also shown is the coupling of the p_x-p_{xm} mode in a large Si nanoparticle placed on an Au/SiO_2 substrate with the excitons in a WS_2 monolayer (blue curve). The experimental setups used to measure the backward and forward scattering of a Si nanoparticle placed on an Au/SiO_2 substrate, which represent also the two excitation schemes of the Si nanoparticle, are schematically illustrated (d) and (e), respectively. Temperature rises induced by a 532-nm laser beam of 1.0 mW in an all-metallic (Au/Au) nanocavity (g) and a hybrid (Si/Au) nanocavity (h). The temperature rises induced by a 800-nm laser beam of 1.0 mW for the all-metallic and hybrid nanocavities are shown in (i) and (j), respectively. The diameters of Au and Si nanoparticles are chosen to be 175 nm and the thickness of the Au film is set to be 50 nm. (For interpretation of the references to colour in this figure legend, the reader is referred to the web version of this article.)

criterion for strong coupling. Similarly, gold (Au) nanorods with different aspect ratios were employed to interact with WS_2 monolayer [22]. Strong plasmon-exciton coupling was revealed by shifting the SPR of the Au nanorod or by varying the exciton energy of WS_2 monolayer. More interestingly, it was demonstrated that the Rabi splitting energy can also be manipulated by changing the polarization angle of the incident light [16]. Unfortunately, the transition from strong to weak coupling regime was not achieved by using this method. Strong plasmon-exciton coupling with a large Rabi splitting energy was also realized in plasmonic nanocavities of other types, such as Au nanodisks [23] and double nanocones [24], and Ag nanotriangles [21]. Other methods that have been proposed to significantly enhance the light-matter interactions in two-dimensional materials and realize perfect absorption of light include the critical coupling with guided resonances [34] and the so-called phase coupled method [35].

From the view point of coupling strength, the small mode volume of plasmonic nanocavities is an advantage over conventional optical cavities. However, the Ohmic loss of plasmonic nanocavities at optical

frequencies leads to the heating of the cavities and the surrounding environment, which affects the stability of two-dimensional TMDCs and the investigation of complex systems. Apart from plasmonic nanoparticles, dielectric nanoparticles with large refractive indices, which support Mie resonances in the visible to near infrared spectral range, were also employed as nanocavities for interacting with TMDCs [32]. For silicon (Si) nanospheres placed on a WS_2 monolayer, weak coupling between nanocavities and excitons was experimentally observed and the coupling strength could be modified by changing the surrounding medium. In Si/WS_2 core–shell structures, which are not feasible from the view point of practical fabrication, strong coupling can be realized [26,36].

In order to enhance the coupling strength, particle-on-film systems were generally employed to reduce the mode volumes of plasmonic nanocavities in which TMDCs were embedded [27–29]. So far, weak and strong coupling has been achieved in all-metallic particle-on-film systems with embedded TMDCs [8,37–39]. Recently, hybrid nanocavities constructed with high-index dielectric nanoparticles and thin metal films have attracted great interest because they can provide strong localization of electric field with reduced Ohmic loss [40,41]. However, the coupling of such hybrid nanocavities with excitons in TMDCs remains unexplored.

In this article, we investigated both numerically and experimentally the optical modes excited in a hybrid nanocavity, which is composed of a high-index dielectric nanoparticle (e.g., a Si nanoparticle) placed on a thin metal film (e.g., an Au film), and their interactions with the excitons in a WS_2 monolayer embedded in the nanocavity. It was found that the coherent interaction of the magnetic dipole (MD) excited in a Si nanoparticle with its mirror image induced by a thin Au film leads to an optical mode with a broadened linewidth. In sharp contrast, the constructive interference of the electric dipole (ED) with its mirror image leads to an optical mode with a narrowed linewidth. In addition, it was revealed by numerical simulation that the enhancement factor in the electric field depends strongly on the excitation scheme of the nanocavity and strong plasmon-exciton coupling can only be achieved by using the optical mode formed by the ED and its mirror image when the nanocavity is excited from the Au film side. This prediction was confirmed by the experimental observation and Rabi splitting of ~72 meV was observed in the forward scattering spectrum of the Si nanoparticle.

2. Physical model and numerical method

The dielectric nanoparticles used to create the hybrid nanocavities are Si nanoparticles with a large refractive index in the visible to near infrared spectral range ($n \sim 3.4$). The scattering spectrum of a typical Si nanoparticle supported by a silica (SiO_2) substrate is shown in Fig. 1a. It consists of the contributions of the ED and MD, corresponding to the two peaks in the scattering spectrum. In principle, a hybrid nanocavity can be constructed by placing a spherical Si nanoparticle on a thin Au film (or an Au/SiO_2 substrate), as shown in Fig. 1b. In order to study plasmon-exciton coupling, one can embed a WS_2 monolayer in the nanocavity so that the excitons in it can be coupled to the plasmons of the nanocavity, as schematically illustrated in Fig. 1c. In practice, the Au film can be deposited on the SiO_2 substrate by using sputtering. The WS_2 monolayer can be firstly grown on a sapphire or silicon substrate and then transferred to the Au film [42]. Si nanoparticles with different diameters can be fabricated by using femtosecond laser ablation and dispersed on the WS_2 monolayer by drop-casting. In this article, we indicated the possibility of realizing strong coupling in such hybrid nanocavities by using numerical simulations based on the finite-difference time-domain (FDTD) technique (FDTD solution, https://www.lumerical.com). The temperature distributions inside the hybrid nanocavities were calculated numerically based on the finite element method (FEM) (COMSOL Multiphysics v5.5, https://www.comsol.com). In the numerical simulations, the thicknesses of the Au film and WS_2 monolayer were chosen to be 50 nm and 1.0 nm, respectively. The dielectric function of Au was taken from the experimental data [43] and those for Si and WS_2 monolayer were taken from previous literatures [44,45]. Non-uniform grids with the minimum size of 0.5 nm in the XY plane and 0.1 nm in the Z direction were used to divide the simulation region, which was enclosed by a perfectly matched layer capable of absorbing all outgoing waves.

In order to describe the coupling between the plasmons in the nanocavity and the excitons in WS_2, we employed a classical coupled oscillator model (COM) which can be expressed as [46–49]:

$$\begin{pmatrix} E_{pl} - \frac{i\Gamma_{pl}}{2} & g \\ g & E_{ex} - \frac{i\Gamma_{ex}}{2} \end{pmatrix} \begin{pmatrix} \alpha \\ \beta \end{pmatrix} = E_{\pm} \begin{pmatrix} \alpha \\ \beta \end{pmatrix} \quad (1)$$

Here, E_{pl} and E_{ex} are the resonant energies of the plasmons and excitons, Γ_{pl} and Γ_{ex} are the damping rates of the plasmons and excitons, α and β are eigen-parameters satisfying $|\alpha|^2 + |\beta|^2 = 1$, g is the coupling strength between plasmons and excitons, which is generally written as [46]:

$$g = \sqrt{N}\mu_e |E_{cav}| \propto \mu_e \sqrt{N/V} \quad (2)$$

Here, N is the number of the excitons within the volume of the optical mode, μ_e is the dipole moment of the excitons, E_{cav} and V are the electric field and mode volume of the nanocavity, respectively. This relationship implies that the mode volume of the nanocavity plays a crucial role in determining the coupling strength between the plasmons and the excitons. For two-dimensional materials, such as the WS_2 monolayer studied in this work, the horizontally-oriented excitons in the WS_2 monolayer interact only with the in-plane electric field of the nanocavity (i.e., E_{xy} in our case).

The energies of the hybrid states $E_{\pm}$ formed by the plasmon-exciton coupling can be derived:

$$E_{\pm} = \frac{E_{pl} + E_{ex}}{2} \pm \frac{\sqrt{\Omega^2 + (E_{pl} - E_{ex})^2}}{2} \quad (3)$$

where the Rabi splitting energy Ω is given by:

$$\Omega = \sqrt{4g^2 - \frac{|\Gamma_{pl} - \Gamma_{ex}|^2}{4}} \quad (4)$$

It is generally thought that plasmon-exciton coupling enters into the strong coupling regime if the following criterion is fulfilled [16,46]:

$$\Omega > \frac{\Gamma_{pl} + \Gamma_{ex}}{2} \text{ or } \Omega > \frac{\Gamma_{pl} - \Gamma_{ex}}{2} \quad (5)$$

3. Sample fabrication and experimental details

The WS_2 monolayer used in this work was synthesized on a Si substrate via chemical vapor deposition and then transferred to an Au/SiO_2 substrate with a 50-nm-thick Au film. The Au film was beforehand deposited on a SiO_2 substrate via vacuum coating and the surface roughness was estimated to be ~ 0.5 nm. The photoluminescence and Raman spectra of the WS_2 monolayer were measured by using the 532-nm laser light (~1 mW) of a Raman spectrometer (inVia, Renishaw).

Si nanoparticles with different diameters were fabricated by using femtosecond laser ablation. A crystalline Si wafer immersed in deionized water was used as the target. The 800-nm femtosecond laser pulses (with a duration of 100 fs and a repetition rate of 1 kHz) delivered by a femtosecond amplifier (Legend, Coherent) was employed to ablate the Si wafer. The aqueous solution of Si nanoparticles was dropped on the Au/SiO_2 substrate and dried naturally. The Si nanoparticles distributed on the WS_2 monolayer were used to create hybrid nanocavities for investigating the plasmon-exciton coupling.

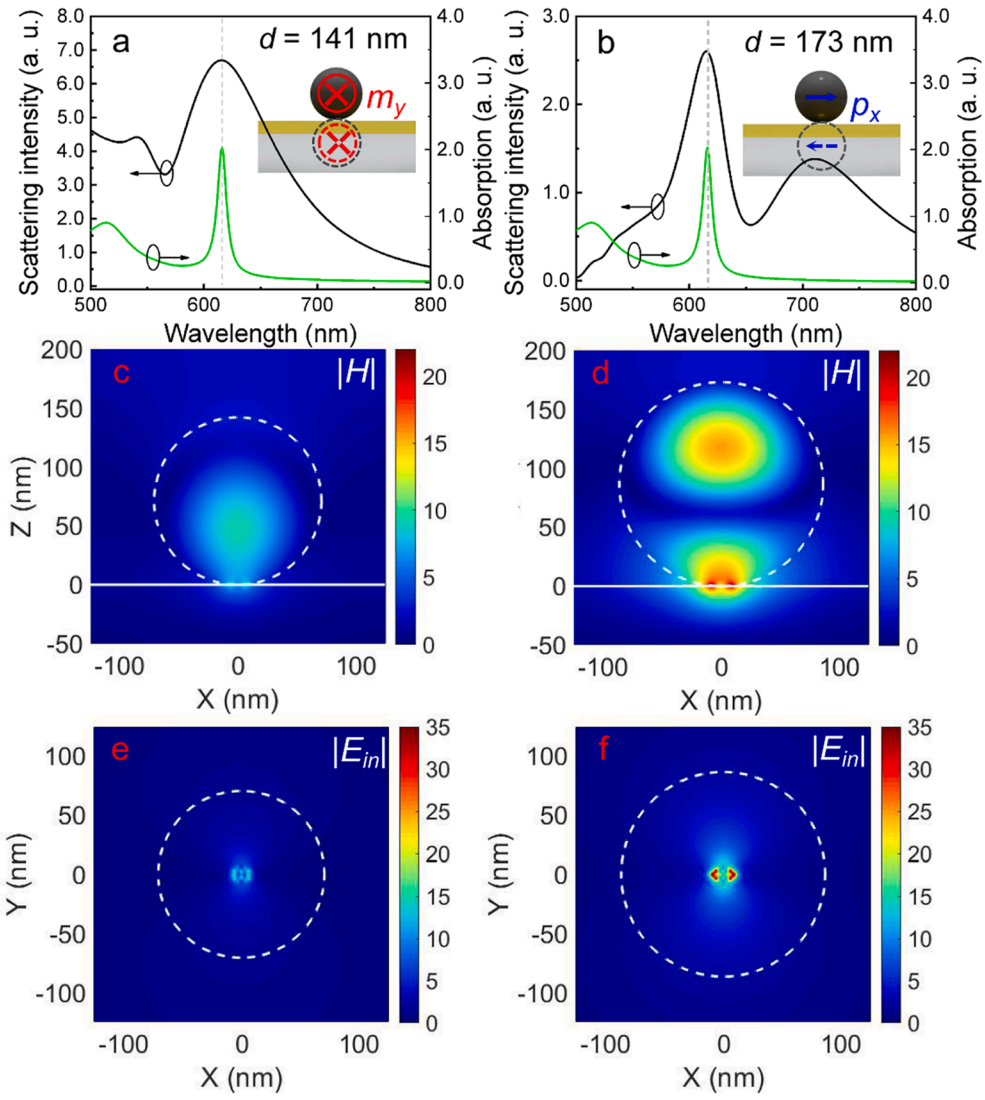

Fig. 2. Backward scattering spectra (solid black curves) calculated for Si nanoparticles with diameters of $d = 141$ nm (a) and $d = 173$ nm (b) placed on an Au/SiO_2 substrate (the excitation scheme shown in Fig. 1(d)). In each case, the absorption spectrum of the WS_2 monolayer (solid green curve) is provided for reference. The MD (m_y) (or ED (p_x)) mode excited in the Si nanoparticle and its mirror image induced by the Au film are shown in the inset. The magnetic field distributions ($|H/H_0|$) in the XZ plane calculated at 615 nm for the two modes are shown in (c) and (d), respectively. The in-plane electric field distributions $|E_{xy}/E_0|$) in the XY plane calculated at 615 nm for the two modes are shown in (e) and (f), respectively. (For interpretation of the references to colour in this figure legend, the reader is referred to the web version of this article.)

4. Results and discussion

We first consider the optical modes excited in the hybrid nanocavity composed of a Si nanoparticle and a thin Au film shown in Fig. 1b. It can be described by using the mirror-image theory proposed previously [40,50–53]. The far-field radiation of the nanocavity arises from the coherent interaction of the Mie resonances supported by the Si nanoparticle with their mirror images induced by the Au film. As depicted in Fig. 1b, the interference of ED and its mirror image, which are antiparallel, leads to a narrowed optical resonance. In contrast, the interference of the MD and its mirror image, which are parallel, results in a broadened optical resonance. In this work, we investigate the coupling of the plasmons excited in these two optical modes with the excitons in the WS_2 monolayer. The resonant wavelengths of the optical modes can be adjusted by varying the diameter of the Si nanoparticle. As schematically shown in Fig. 1c, mode splitting can be observed when the wavelengths of the plasmons and excitons coincide.

In practice, the hybrid nanocavity can be excited by two schemes in order to experimentally observe the plasmon-exciton coupling, as illustrated in Fig. 1d and e. Although the mirror-image theory is applicable in both cases, the enhancement factor of the electric field in the nanocavity exhibits a strong dependence on the excitation scheme, as demonstrated latter.

Before examining the optical properties of the hybrid nanocavity, we make a comparison between the hybrid nanocavity proposed in this work and an all-metallic nanocavity commonly used in previous studies in the ohmic heating induced by laser light. We calculated the temperature rises induced in the two nanocavities by using laser beams with a fixed power of 1.0 mW at two wavelengths of 532 and 800 nm, as shown in Fig. 1g–j. In both cases, it is found that the temperature rise in the all-metallic nanocavity composed of an Au nanoparticle and an Au film is higher than that in the hybrid nanocavity, implying a mitigated ohmic heating in the latter case.

We first calculated the backward scattering spectra of two Si nanoparticles (i.e., with the excitation scheme shown in Fig. 1d) with different diameters of $d = 141$ nm and $d = 173$ nm, as shown in Fig. 2a and b. In the former case, the optical resonance originates from the interference of the MD (m_y) and its mirror image (m_{ym}), which we refer to as m_y/m_{ym} mode in the following. Similarly, the optical resonance in the latter case arises from the interference of the ED (p_x) and its mirror image (p_{xm}), which we denote as p_x/p_{xm} mode hereafter. In both cases, the resonant wavelength of the optical mode coincides with that of the excitons in the WS_2 monolayer (615 nm). It is noticed, however, that the linewidth of the m_y/m_{ym} mode is broader than that of the p_x/p_{xm} mode because of the reason stated above. In Fig. 2c and d, we present the magnetic field distributions in the XZ plane calculated for the two modes (or two nanocavities) at their resonant wavelengths (615 nm). For the m_y/m_{ym} mode, the maximum magnetic field appears in the Si

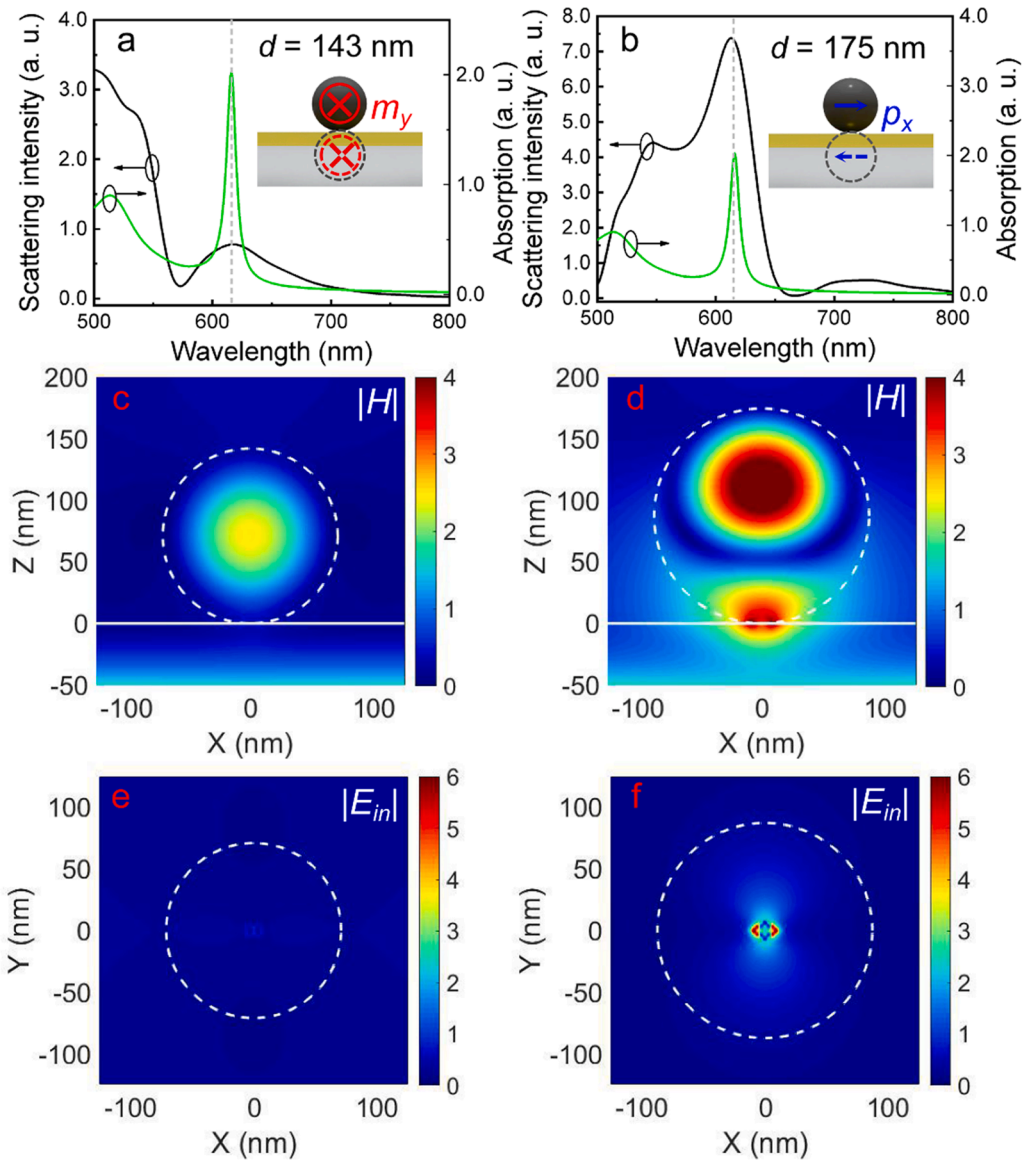

Fig. 3. Forward scattering spectra (solid black curves) calculated for Si nanoparticles with diameters of $d = 143$ nm (a) and $d = 175$ nm (b) placed on an Au/SiO_2 substrate (the excitation scheme shown in Fig. 1(e)). In each case, the absorption spectrum of WS_2 monolayer (solid green curve) is provided for reference. The MD (m_y) (or ED (p_x)) mode excited in the Si nanoparticle and its mirror image induced by the Au film are shown in the inset. The magnetic field distributions ($|H/H_0|$) in the XZ plane calculated at 615 nm for the two modes are shown in (c) and (d), respectively. The in-plane electric field distributions $|E_{xy}/E_0|$) in the XY plane calculated at 615 nm for the two modes are shown in (e) and (f), respectively. (For interpretation of the references to colour in this figure legend, the reader is referred to the web version of this article.)

nanoparticle. In sharp contrast, the maximum magnetic field for the p_x/p_{xm} mode is observed in the region between the Si nanoparticle and the Au film.

As discussed above, the horizontally-oriented excitons in the WS_2 monolayer can only interact with the in-plane electric field (E_{xy}) of the nanocavity. In Fig. 2e and f, we compare the in-plane electric field distributions in the XY plane calculated for the two modes. It can be seen that the enhancement factor in the electric field for the p_x/p_{xm} mode (~35) is much larger than that for the m_y/m_{ym} mode (~15). In addition, the in-plane electric field distributions of the two modes are apparently different.

Now we consider another excitation scheme of the nanocavity in which the forward scattering spectra of the Si nanoparticles are detected, as shown in Fig. 1e. The calculated forward scattering spectra for two Si nanoparticles with different diameters are shown in Fig. 3a and b. To design nanocavities with optical modes resonant with the excitons of the WS_2 monolayer (~615 nm), the diameters of Si nanoparticles are chosen to be $d = 143$ nm and $d = 175$ nm, respectively. In the former case, the scattering intensity of the m_y/m_{ym} mode is very weak. In comparison, a much stronger scattering intensity is observed for the p_x/p_{xm} mode in the latter case. In Fig. 3c and d, we present the magnetic field distributions in the XZ plane for the two modes at their resonant wavelengths (615 nm). For the m_y/m_{ym} mode, the maximum magnetic field is located at the center of the Si nanoparticle. Differently, the maximum magnetic field is observed at the contacting point between the Si nanoparticle and the Au film for the p_x/p_{xm} mode. It is remarkable, however, that the enhancement factors of the electric field in both cases are much smaller than those observed in the first excitation scheme, especially for the m_y/m_{ym} mode.

Now we investigate the plasmon-exciton coupling in the four nanocavities, whose optical properties have been discussed above, by inserting a WS_2 monolayer in each cavity. In Fig. 4a and b, we present the backward scattering spectra calculated for two nanocavities composed of Si nanoparticles with $d = 141$ nm (m_y/m_{ym} mode) and $d = 173$ nm (p_x/p_{xm} mode) with an embedded WS_2 monolayer. The backward scattering spectra of the nanocavities in the absence of the WS_2 monolayer are also provided for comparison. The linewidth (full width at half maximum) of the absorption peak of the WS_2 monolayer, which reflects the damping rate of the excitons in the WS_2 monolayer, is estimated to be ~ 45 meV. This value is close to those reported previously [29,38]. In both cases, mode splitting due to plasmon-exciton coupling is observed in the scattering spectra. The splitting energy is estimated to be $\Omega \sim 97$ meV in the former nanocavity and $\Omega \sim 65$ meV in the latter one. Although a large energy splitting of ~ 97 meV is observed in the

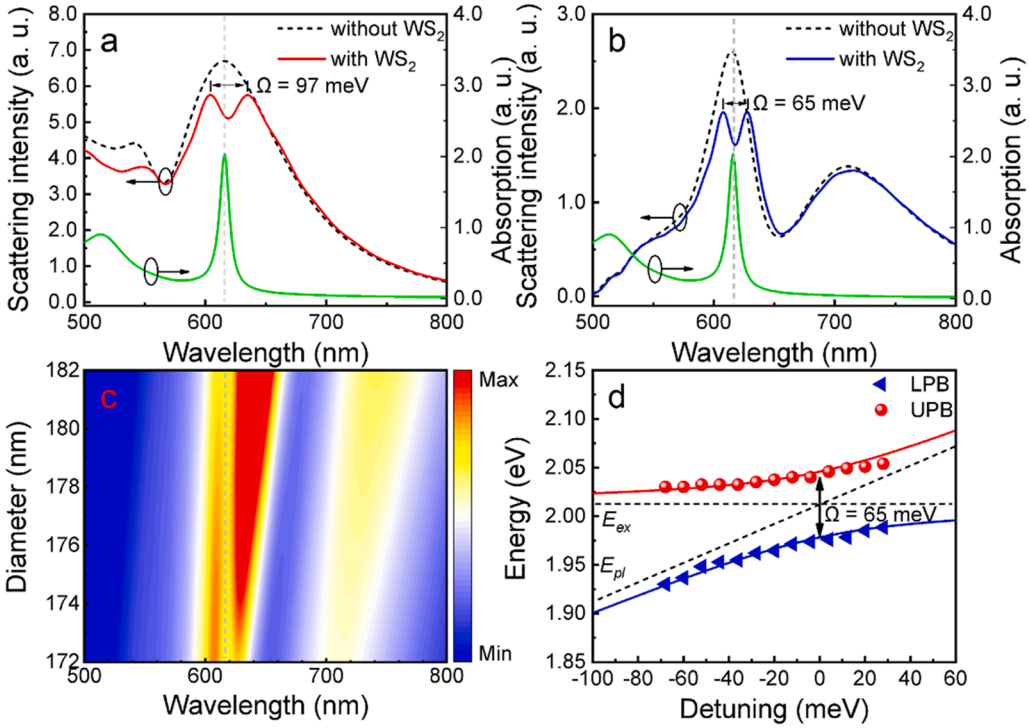

Fig. 4. Backward scattering spectra calculated for the hybrid nanocavities composed of Si nanoparticles with diameters $d = 141$ nm (a) and $d = 173$ nm (b) without (dashed black curves) and with (solid red/blue curves) an embedded WS_2 monolayer. In each case, the absorption spectrum of the WS_2 monolayer (solid green curve) is provided for reference. (c) Two-dimensional backward scattering spectra calculated for Si nanoparticles with different diameters (from $d = 172$ to $d = 182$ nm). (d) Resonant energies for the upper and lower plexciton branches extracted from the numerical simulations (colored symbols) and the fittings based on the coupled oscillator model (colored curves). (For interpretation of the references to colour in this figure legend, the reader is referred to the web version of this article.)

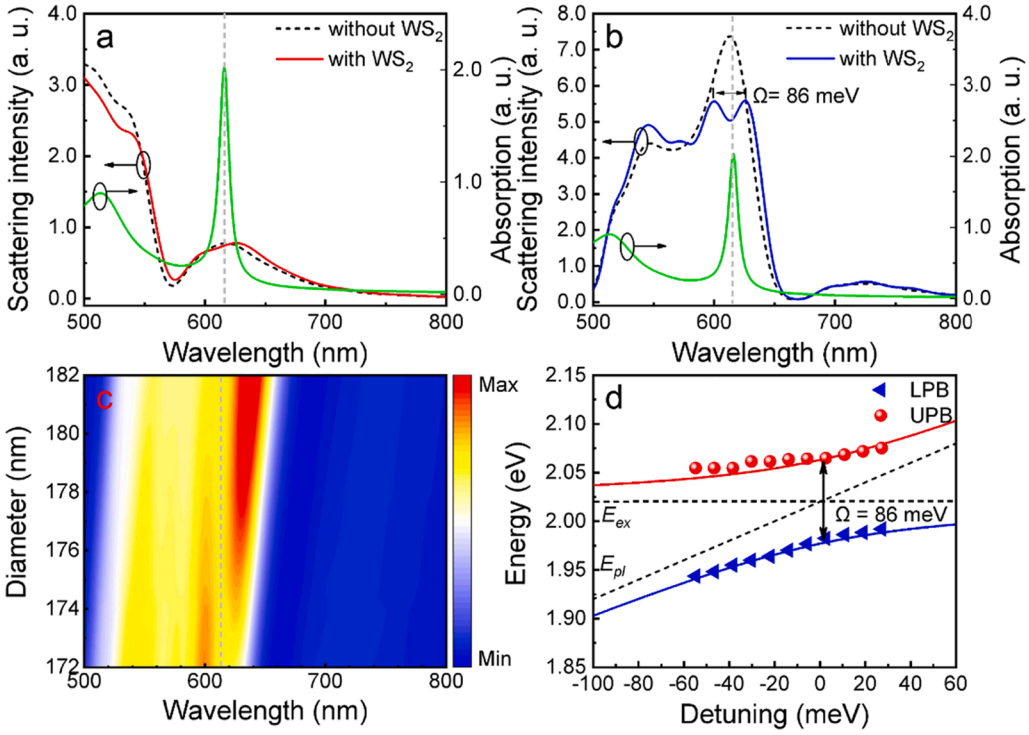

Fig. 5. Forward scattering spectra calculated for the hybrid nanocavities composed of Si nanoparticles with diameters $d = 143$ nm (a) and $d = 175$ nm (b) without (dashed black curves) and with (solid red/blue curves) an embedded WS_2 monolayer. In each case, the absorption spectrum of the WS_2 monolayer (solid green curve) is provided for reference. (c) Two-dimensional backward scattering spectra calculated for Si nanoparticles with different diameters (from $d = 172$ to $d = 182$ nm). (d) Resonant energies for the upper and lower plexciton branches extracted from the numerical simulations (colored symbols) and the fittings based on the coupled oscillator model (colored curves). (For interpretation of the references to colour in this figure legend, the reader is referred to the web version of this article.)

nanocavity with $d = 141$ nm, the plasmon-exciton coupling is still in the weak coupling regime because the linewidth (or the damping rate) of the optical mode is also large (~320 meV). For the nanocavity with $d = 173$ nm, the criterion for strong coupling (Eq. (5)) is also not satisfied because of the small energy splitting. In order to gain a deep insight into the plasmon-exciton coupling in such nanocavities, we calculated the backward scattering spectra for nanocavities composed of Si nanoparticles with diameters ranging from 172 to 182 nm, as shown in Fig. 4c. An anti-crossing behavior originating from the energy splitting is clearly observed, verifying the existence of plasmon-exciton coupling. In Fig. 4d, we present the resonant energies of the two scattering peaks obtained for nanocavities composed of Si nanoparticles with different diameters as a function of the detuning energy from the exciton energy. The fitting results based on COM (Eq. (3)) are also provided, which give the lower and upper plexciton branches of the mixed states.

Similarly, we also examined the forward scattering spectra for the

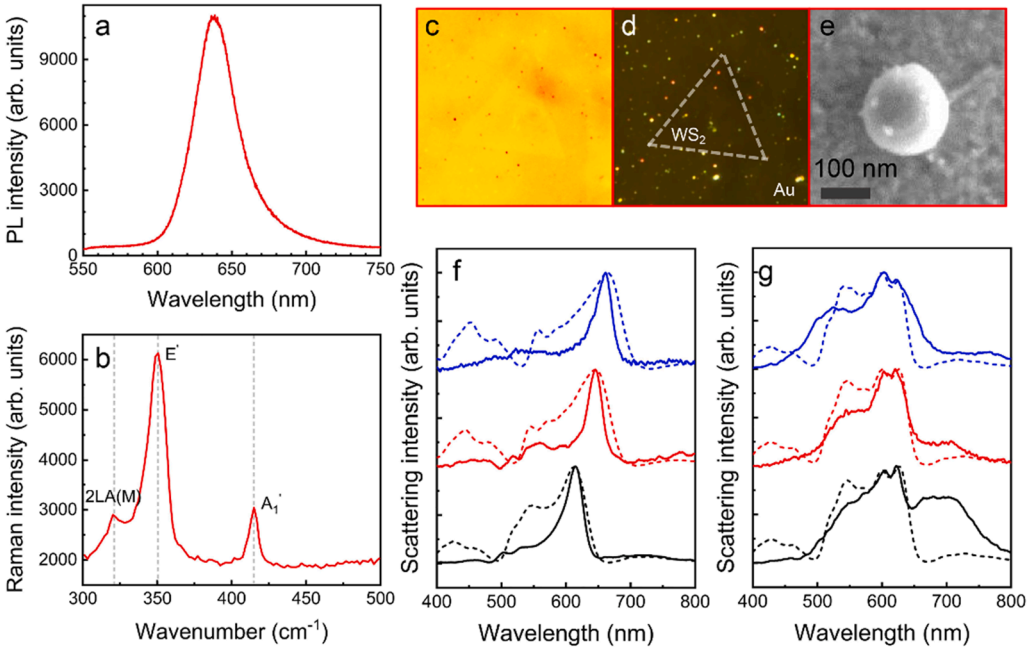

Fig. 6. (a) Photoluminescence spectrum measured for the WS_2 monolayer excited by using 532-nm laser light. (b) Raman scattering spectrum measured for the WS_2 monolayer. (c) Bright-field image taken for the WS_2 monolayer and Si nanoparticles located on the Au film. (d) Dark-field microscope image taken for the WS_2 monolayer and Si nanoparticles located on the Au film. (e) SEM image of a typical Si nanoparticle located on the Au film. (f) Forward scattering spectra measured for three Si nanoparticles with different diameters located on the Au film. (g) Forward scattering spectra measured for three Si nanoparticles with similar diameters located on the WS_2 monolayer. In (f) and (g), the simulated scattering spectra (dashed curves) with normal incidence are also provided for comparison.

two nanocavities with $d = 143$ nm (m_y/m_{ym} mode) and $d = 175$ nm (p_x/p_{xm} mode) with an embedded WS_2 monolayer, as shown in Fig. 5a and b. The forward scattering spectra of the nanocavities without the WS_2 monolayer are also provided for comparison. For the nanocavity with $d = 143$ nm, the plasmon-exciton coupling is too weak to be resolved in the scattering spectrum. This behavior is in good agreement with the small enhancement factor of the electric field observed for this nanocavity (see Fig. 3e). In sharp contrast, a large energy splitting of $\Omega \sim 86$ meV is found for the nanocavity with $d = 175$ nm. Similarly, the anti-crossing behavior is revealed in the two-dimensional scattering spectra calculated for nanocavities composed of Si nanoparticles with diameters ranging from 172 to 182 nm, as shown in Fig. 5c. The lower and upper plexction branches can be obtained by fitting the simulation results with COM (Eq. (3)), as shown in Fig. 5d. Although the splitting energy in this case (forward scattering) is slightly smaller than that observed in the nanocavity with $d = 141$ nm (backward scattering, see Fig. 4a), the criterion for strong coupling is fulfilled because of the significantly reduced linewidth (~120 meV) of the p_x/p_{xm} mode. The linewidth of the plasmons in this case is extracted by fitting the scattering spectrum with multiple Lorentz lineshapes and verified by the linewidth of a larger Si nanoparticle [40] (see Si nanoparticle with $d \sim 180$ nm). It implies that strong plasmon-exciton coupling can be realized in this nanocavity when it is excited from the Au film side (i.e., forward scattering). Although the enhancement factor of the electric field is not large in this case, we think that the small mode volume of the nanocavity is responsible for the achievement of strong plasmon-exciton coupling.

We have simulated the forward and backward scattering spectra of hybrid nanocavities composed of Au film of different thickness and the compared the in-plane electric field distributions in these nanocavities, as shown in Fig. S1. It is noticed that the in-plane electric field decreases with increasing thickness of the Au film in the forward scattering case while a reversed situation is observed in the backward scattering case (see Fig. S1a − f). When the thickness of the Au film becomes smaller than 20 nm, the mirror image theory used to describe the scattering of the Si nanoparticle is no longer applicable. In this case, the p_x/p_{xm} mode originating from the interference of the ED and its mirror image disappears completely in the scattering spectrum. Differently, a significant reduction of the in-plane electric field is found for nanocavities with Au films thicker than 80 nm. In this case, the coupling strength is too weak and energy splitting is invisible (see Fig. S1g). As for the backward scattering, the situation for a nanocavity with a very thin Au film is quite similar to that observed in the forward scattering. There is no p_x/p_{xm} mode in such a nanocavity. In comparison, the increase in the thickness of the Au film does not lead to apparent change in the in-plane electric field. As a result, the coupling strength remains nearly unchanged (see Fig. S1h).

In order to experimentally demonstrate the strong plasmon-exciton coupling predicted above, we have fabricated Si nanoparticles with different diameters by using femtosecond laser ablation. They were dispersed on a WS_2 monolayer which was beforehand transferred onto the Au film. In order to confirm the monolayer nature of the WS_2 film, we performed photoluminescence and Raman measurements for it, as shown in Fig. 6a and b. The characteristics of photoluminescence and Raman spectra of the WS_2 film agree well with those reported previously for WS_2 monolayer [54]. In Fig. 6c and d, we show the bright- and dark-field microscope images of Si nanoparticles distributed on the Au film recorded by using a coupled charge device (CCD). The scanning electron microscopy (SEM) image of a typical Si nanoparticle is shown in Fig. 6e. In Fig. 6c, one can easily identify the triangular WS_2 film. It will help us to locate Si nanoparticles distributed on the WS_2 monolayer in the dark-field image, as shown in Fig. 6d. The forward scattering spectra measured for three Si nanoparticles on the Au film (i.e., hybrid nanocavities without the WS_2 monolayer) are shown in Fig. 6f. The simulated scattering spectra, from which the diameters of the Si nanoparticles can be extracted, are also provided for comparison. In each case, the forward scattering of a Si nanoparticle located on the Au film exhibits a resonance with a narrow linewidth of ~ 120 meV, corresponding to the radiation of the p_x/p_{xm} mode. The resonant wavelength depends on the diameter of the Si nanoparticle. These two features agree well with those predicted in the simulation results. The discrepancy between the measured and simulated scattering spectra is caused mainly by the difference in the incidence angle, as shown in Fig. S2. Here, we provide the simulated scattering spectra obtained with a normal incidence because the simulation of a scattering spectrum resulting from an oblique incidence takes a much longer time. In the experiments, however, the scattering spectra were obtained with incidence angles ranging from ~ 30° to ~ 60° in the dark-field microscope. Nevertheless, the measured scattering spectra agree with the simulated ones except the narrowing of the linewidth. In Fig. 6h, we present the scattering spectra measured for three Si nanoparticles located on the WS_2 monolayer. Clearly, energy

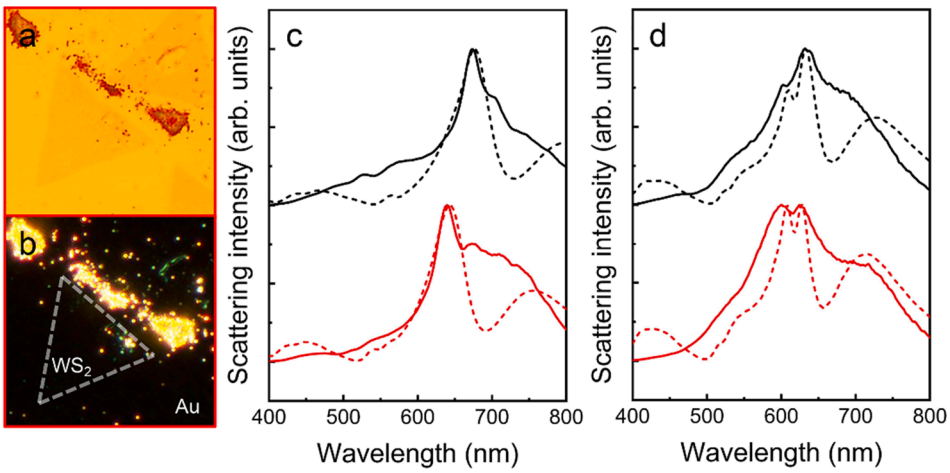

Fig. 7. (a) Bright- and (b) dark-field microscope images taken for the WS_2 monolayer and Si nanoparticles located on the Au film. (c) Backward scattering spectra measured for two Si nanoparticles with different diameters located on the Au film. (d) Backward scattering spectra measured for two Si nanoparticles with similar diameters located on the WS_2 monolayer. In (c) and (d), the simulated scattering spectra (dashed curves) with normal incidence are also provided for comparison.

splitting due to plasmon-exciton coupling was observed in all cases and the splitting energy was estimated to be $\Omega \sim 72$ meV, which is close to the value obtained in the numerical simulation. Considering that the linewidth (or damping rate) of the optical mode is also reduced in the case of oblique incidence, the coupling strength is close to strong coupling criterion. In Fig. 6d, we also provide the simulated scattering spectra and they are qualitatively agreement with the measured results. Therefore, we think the measured scattering spectra provide direct evidence for the achievement of strong plasmon-exciton coupling in the hybrid nanocavity by deliberately choosing the optical mode and the excitation scheme.

For the completeness of the study, we also performed backward scattering measurements for the hybrid nanocavities without and with an embedded WS_2 monolayer although strong plasmon-exciton coupling is not expected for this excitation scheme based on the numerical simulations presented above. It should be pointed out that in most cases energy splitting was not observed simultaneously in both the forward and backward scattering spectra of a hybrid nanocavity due to the small difference in the resonant wavelength of the p_x/p_{xm} mode, as shown in Fig. S3. In Fig. 7a and b, we show the bright- and dark-field microscope images of a WS_2 monolayer and Si nanoparticles located on the Au film. In Fig. 7c, we present the backward scattering spectra measured for two Si nanoparticles located on the Au film with different resonant wavelengths for the p_x/p_{xm} mode. The simulated scattering spectra at the normal incidence are also provided for comparison. In Fig. 7d, we present the backward scattering spectra measured for two Si nanoparticles located on the WS_2 monolayer. In each case, the resonant wavelength of the p_x/p_{xm} mode is close to the exciton energy of the WS_2 monolayer. As expected, one can see energy splitting in both cases. Since a broadening of the linewidth was found in the measured result as compared with the simulated one, the measured energy splitting was slightly larger than the simulated one. This is also caused by the difference in the incidence angle in the measurement (~60°) and simulation (0°) (see Fig. S2). Although the energy splitting is increased in this case, the criterion for strong coupling is still not fulfilled because of the broader linewidth.

In experiments, mode splitting can only be observed in hybrid nanocavities whose resonances are close to the exciton energy of the WS_2 monolayer (~615 nm). A small deviation of the nanocavity resonance away from the exciton energy will lead to a rapid decrease of coupling strength and the disappearance of the mode splitting (i.e., the scattering dip is not resolved in the scattering spectrum). Owing to the limit number of Si nanoparticles dispersed on the WS_2 monolayer (see Fig. 6d and Fig. 7b), it remains a big challenge to extract the dispersion curve by exploiting the size distribution of Si nanoparticles.

5. Conclusions

In summary, we have proposed for the first time the use of a high-index dielectric (Si) nanoparticle and a thin metal (Au) film to construct a hybrid nanocavity and investigated systematically the optical modes supported by the nanocavity. The p_x/p_{xm} and m_y/m_{ym} modes originating from the coherent interaction of the ED and MD excited in the Si nanoparticle and their mirror images induced by the Au film are employed to interact with the excitons in the WS_2 monolayer. It was found that optical properties of the p_x/p_{xm} and m_y/m_{ym} modes, including the electric field enhancement and mode volume, depend strong on the excitation scheme of the nanocavity. It was revealed that strong plasmon-exciton coupling can only be achieved by using the p_x/p_{xm} mode excited from the Au film side because of the significantly reduced linewidth and mode volume. Owing to the mitigated ohmic heating of the hybrid nanocavity, such a configuration is quite suitable to study the enhanced linear and nonlinear optical resonances of the two-dimensional materials embedded in the nanocavity, such as single- and multiphoton luminescence and second harmonic generation. In addition, one can consider the excitation of the hybrid nanocavity with other schemes (such as surface plasmon polaritons generated on the surface of the Au film), which may lead to a larger enhancement in the electric field and a stronger plasmon-exciton coupling strength. By using various two-dimensional materials embedded in the nanocavity as gain materials, nanoscale photonic devices such as lasers or spacers with small mode volumes could be constructed. Therefore, our findings indicate the possibility for realizing strong light-matter interaction in hybrid nanocavities and open new horizons for designing nanoscale photonic devices.

CRediT authorship contribution statement

S. Lan, H. Huang, and F. Deng conceived the idea. H. Huang, F. Deng and S. Li carried out the optical measurements and numerical simulations. S. Lan, H. Huang, F. Deng, J. Xiang and S. Li analyzed the data and wrote the manuscript. S. Lan supervised the project. All the authors read and commented on the manuscript.

Declaration of Competing Interest

The authors declare that they have no known competing financial interests or personal relationships that could have appeared to influence the work reported in this paper.

Acknowledgements

This work was financially supported by the National Natural Science Foundation of China (Grant Nos. 11674110 and 11874020) and the Natural Science Foundation of Guangdong Province, China (Grant Nos. 2016A030308010).

Appendix A. Supplementary material

Supplementary data to this article can be found online at https://doi.org/10.1016/j.apsusc.2020.148660.

References

[1] S.K. Rajendran, M. Wei, H. Ohadi, A. Ruseckas, G.A. Turnbull, I.D.W. Samuel, Low threshold polariton lasing from a solution-processed organic semiconductor in a planar microcavity, Adv. Opt. Mater. 7 (2019).
[2] J.A. Hutchison, A. Liscio, T. Schwartz, A. Canaguier-Durand, C. Genet, V. Palermo, P. Samori, T.W. Ebbesen, Tuning the work-function via strong coupling, Adv. Mater. 25 (2013) 2481–2485.
[3] M.Y. Musa, M. Renuka, X. Lin, R. Li, H. Wang, E. Li, B. Zhang, H. Chen, Confined transverse electric phonon polaritons in hexagonal boron nitrides, 2D Mater. 5 (2017).
[4] T.T. Tran, D. Wang, Z.Q. Xu, A. Yang, M. Toth, T.W. Odom, I. Aharonovich, Deterministic coupling of quantum emitters in 2D materials to plasmonic nanocavity arrays, Nano Lett. 17 (2017) 2634–2639.
[5] M. Blauth, J. Harms, M. Prechtl, J. Finley, M. Kaniber, Enhanced optical activity of atomically thin $MoSe_2$ proximal to nanoscale plasmonic slot-waveguides, 2D Mater. 4 (2017), 021011.
[6] S. Hou, A. Xie, Z. Xie, L.Y.M. Tobing, J. Zhou, L. Tjahjana, J. Yu, C. Hettiarachchi, D. Zhang, C. Dang, E.H.T. Teo, M.D. Birowosuto, H. Wang, Concurrent inhibition and redistribution of spontaneous emission from all inorganic perovskite photonic crystals, ACS Photonics 6 (2019) 1331–1337.
[7] M.H. Tahersima, M.D. Birowosuto, Z. Ma, W.C. Coley, M.D. Valentin, S. Naghibi Alvillar, I.H. Lu, Y. Zhou, I. Sarpkaya, A. Martinez, I. Liao, B.N. Davis, J. Martinez, D. Martinez-Ta, A. Guan, A.E. Nguyen, K. Liu, C. Soci, E. Reed, L. Bartels, V. J. Sorger, Testbeds for transition metal dichalcogenide photonics: efficacy of light emission enhancement in monomer vs dimer nanoscale antennae, ACS Photonics 4 (2017) 1713–1721.
[8] Y. Zhang, W. Chen, T. Fu, J. Sun, D. Zhang, Y. Li, S. Zhang, H. Xu, Simultaneous surface-enhanced resonant Raman and Fluorescence Spectroscopy of Monolayer $MoSe_2$: Determination of Ultrafast Decay Rates in Nanometer Dimension, Nano Lett. 19 (2019) 6284–6291.
[9] C. Ma, J. Yan, Y. Huang, G. Yang, Photoluminescence manipulation of WS_2 flakes by an individual Si nanoparticle, Mater. Horiz. 6 (2019) 97–106.
[10] I. Chiorescu, P. Bertet, K. Semba, Y. Nakamura, C.J. Harmans, J.E. Mooij, Coherent dynamics of a flux qubit coupled to a harmonic oscillator, Nature 431 (2004) 159–162.
[11] D.G. Lidzey, D. Bradley, M. Skolnick, T. Virgili, S. Walker, D. Whittaker, Strong exciton–photon coupling in an organic semiconductor microcavity, Nature 395 (1998) 53.
[12] F.C. Spano, Optical microcavities enhance the exciton coherence length and eliminate vibronic coupling in J-aggregates, J. Chem. Phys. 142 (2015), 184707.
[13] F. Barachati, J. Simon, Y.A. Getmanenko, S. Barlow, S.R. Marder, S. Kéna-Cohen, Tunable Third-Harmonic Generation from Polaritons in the Ultrastrong Coupling Regime, ACS Photonics 5 (2017) 119–125.
[14] A. Bisht, J. Cuadra, M. Wersall, A. Canales, T.J. Antosiewicz, T. Shegai, Collective Strong Light-Matter Coupling in Hierarchical Microcavity-Plasmon-Exciton Systems, Nano Lett. 19 (2019) 189–196.
[15] H. Wang, Y. Ke, N. Xu, R. Zhan, Z. Zheng, J. Wen, J. Yan, P. Liu, J. Chen, J. She, Y. Zhang, F. Liu, H. Chen, S. Deng, Resonance Coupling in Silicon Nanosphere-J-Aggregate Heterostructures, Nano Lett. 16 (2016) 6886–6895.
[16] A.E. Schlather, N. Large, A.S. Urban, P. Nordlander, N.J. Halas, Near-field mediated plexcitonic coupling and giant Rabi splitting in individual metallic dimers, Nano Lett. 13 (2013) 3281–3286.
[17] E. Eizner, O. Avayu, R. Ditcovski, T. Ellenbogen, Aluminum Nanoantenna Complexes for Strong Coupling between Excitons and Localized Surface Plasmons, Nano Lett. 15 (2015) 6215–6221.
[18] J. Bellessa, C. Bonnand, J.C. Plenet, J. Mugnier, Strong coupling between surface plasmons and excitons in an organic semiconductor, Phys. Rev. Lett. 93 (2004), 036404.
[19] H. Yang, J. Yao, X.-W. Wu, D.-J. Wu, X.-J. Liu, Strong Plasmon–Exciton–Plasmon Multimode Couplings in Three-Layered Ag–J-Aggregates–Ag Nanostructures, J. Phys. Chem. C 121 (2017) 25455–25462.
[20] D. Zheng, S. Zhang, Q. Deng, M. Kang, P. Nordlander, H. Xu, Manipulating Coherent Plasmon-Exciton Interaction in a Single Silver Nanorod on Monolayer WSe_2, Nano Lett. 17 (2017) 3809–3814.
[21] J. Cuadra, D.G. Baranov, M. Wersall, R. Verre, T.J. Antosiewicz, T. Shegai, Observation of Tunable Charged Exciton Polaritons in Hybrid Monolayer WS_2-Plasmonic Nanoantenna System, Nano Lett. 18 (2018) 1777–1785.
[22] J. Wen, H. Wang, W. Wang, Z. Deng, C. Zhuang, Y. Zhang, F. Liu, J. She, J. Chen, H. Chen, S. Deng, N. Xu, Room-Temperature Strong Light-Matter Interaction with Active Control in Single Plasmonic Nanorod Coupled with Two-Dimensional Atomic Crystals, Nano Lett. 17 (2017) 4689–4697.
[23] M. Geisler, X. Cui, J. Wang, T. Rindzevicius, L. Gammelgaard, B.S. Jessen, P.A. D. Gonçalves, F. Todisco, P. Bøggild, A. Boisen, M. Wubs, N.A. Mortensen, S. Xiao, N. Stenger, Single-Crystalline Gold Nanodisks on WS_2 Mono- and Multilayers for Strong Coupling at Room Temperature, ACS Photonics 6 (2019) 994–1001.
[24] M. Stuhrenberg, B. Munkhbat, D.G. Baranov, J. Cuadra, A.B. Yankovich, T. J. Antosiewicz, E. Olsson, T. Shegai, Strong Light-Matter Coupling between Plasmons in Individual Gold Bi-pyramids and Excitons in Mono- and Multilayer WSe_2, Nano Lett. 18 (2018) 5938–5945.
[25] M. Wang, A. Krasnok, T. Zhang, L. Scarabelli, H. Liu, Z. Wu, L.M. Liz-Marzan, M. Terrones, A. Alu, Y. Zheng, Tunable Fano Resonance and Plasmon-Exciton Coupling in Single Au Nanotriangles on Monolayer WS_2 at Room Temperature, Adv. Mater. 30 (2018), e1705779.
[26] S. Lepeshov, M. Wang, A. Krasnok, O. Kotov, T. Zhang, H. Liu, T. Jiang, B. Korgel, M. Terrones, Y. Zheng, A. Alu, Tunable Resonance Coupling in Single Si Nanoparticle-Monolayer WS_2 Structures, ACS Appl. Mater. Interfaces 10 (2018) 16690–16697.
[27] T. Song, Z. Chen, W. Zhang, L. Lin, Y. Bao, L. Wu, Z.K. Zhou, Compounding Plasmon(-)Exciton Strong Coupling System with Gold Nanofilm to Boost Rabi Splitting, Nanomaterials (Basel) 9 (2019).
[28] S. Hou, L.Y.M. Tobing, X. Wang, Z. Xie, J. Yu, J. Zhou, D. Zhang, C. Dang, P. Coquet, B.K. Tay, M.D. Birowosuto, E.H.T. Teo, H. Wang, Manipulating Coherent Light-Matter Interaction: Continuous Transition between Strong Coupling and Weak Coupling in MoS_2 Monolayer Coupled with Plasmonic Nanocavities, Adv. Opt. Mater. 7 (2019).
[29] X. Han, K. Wang, X. Xing, M. Wang, P. Lu, Rabi Splitting in a Plasmonic Nanocavity Coupled to a WS_2 Monolayer at Room Temperature, ACS Photonics 5 (2018) 3970–3976.
[30] G. Wang, A. Chernikov, M.M. Glazov, T.F. Heinz, X. Marie, T. Amand, B. Urbaszek, Colloquium: Excitons in atomically thin transition metal dichalcogenides, Rev. Mod. Phys. 90 (2018).
[31] K.F. Mak, J. Shan, Photonics and optoelectronics of 2D semiconductor transition metal dichalcogenides, Nat. Photonics 10 (2016) 216–226.
[32] S. Lepeshov, A. Krasnok, A. Alu, Enhanced excitation and emission from 2D transition metal dichalcogenides with all-dielectric nanoantennas, Nanotechnology 30 (2019), 254004.
[33] A. Krasnok, S. Lepeshov, A. Alu, Nanophotonics with 2D transition metal dichalcogenides [Invited], Opt. Exp. 26 (2018) 15972–15994.
[34] H. Li, M. Qin, L. Wang, X. Zhai, R. Ren, J. Hu, Total absorption of light in monolayer transition-metal dichalcogenides by critical coupling, Opt. Exp. 25 (2017) 31612–31621.
[35] H. Li, C. Ji, Y. Ren, J. Hu, M. Qin, L. Wang, Investigation of multiband plasmonic metamaterial perfect absorbers based on graphene ribbons by the phase-coupled method, Carbon 141 (2019) 481–487.
[36] H. Wang, J. Wen, W. Wang, N. Xu, P. Liu, J. Yan, H. Chen, S. Deng, Resonance Coupling in Heterostructures Composed of Silicon Nanosphere and Monolayer WS_2: A Magnetic-Dipole-Mediated Energy Transfer Process, ACS Nano (2019).
[37] J. Sun, H. Hu, D. Zheng, D. Zhang, Q. Deng, S. Zhang, H. Xu, Light-Emitting Plexciton: Exploiting Plasmon-Exciton Interaction in the Intermediate Coupling Regime, ACS Nano 12 (2018) 10393–10402.
[38] J. Qin, Y.H. Chen, Z. Zhang, Y. Zhang, R.J. Blaikie, B. Ding, M. Qiu, Revealing Strong Plasmon-Exciton Coupling between Nanogap Resonators and Two-Dimensional Semiconductors at Ambient Conditions, Phys. Rev. Lett. 124 (2020), 063902.
[39] F. Deng, H. Liu, L. Xu, S. Lan, A.E. Miroshnichenko, Strong Exciton-Plasmon Coupling in a WS_2 Monolayer on Au Film Hybrid Structures Mediated by Liquid Ga Nanoparticles, Laser Photonics Rev. (2020) 1900420.
[40] H. Li, Y. Xu, J. Xiang, X.F. Li, C.Y. Zhang, S.L. Tie, S. Lan, Exploiting the interaction between a semiconductor nanosphere and a thin metal film for nanoscale plasmonic devices, Nanoscale 8 (2016) 18963–18971.
[41] Z. Huang, J. Wang, Z. Liu, G. Xu, Y. Fan, H. Zhong, B. Cao, C. Wang, K. Xu, Strong-Field-Enhanced Spectroscopy in Silicon Nanoparticle Electric and Magnetic Dipole Resonance near a Metal Surface, J. Phys. Chem. C 119 (2015) 28127–28135.
[42] B. Li, Y. He, S. Lei, S. Najmaei, Y. Gong, X. Wang, J. Zhang, L. Ma, Y. Yang, S. Hong, J. Hao, G. Shi, A. George, K. Keyshar, X. Zhang, P. Dong, L. Ge, R. Vajtai, J. Lou, Y. J. Jung, P.M. Ajayan, Scalable Transfer of Suspended Two-Dimensional Single Crystals, Nano Lett. 15 (2015) 5089–5097.
[43] P.B. Johnson, R.W. Christy, Optical Constants of the Noble Metals, Phy. Rev. B 6 (1972) 4370–4379.
[44] Palik, D. Edward, Handbook of optical constants of solids, Academic Press, 1985.
[45] Y. Li, A. Chernikov, X. Zhang, A. Rigosi, H.M. Hill, A.M. van der Zande, D. A. Chenet, E.-M. Shih, J. Hone, T.F. Heinz, Measurement of the optical dielectric function of monolayer transition-metal dichalcogenides: MoS_2, $MoSe_2$, WS_2, and WSe_2, Phy. Rev. B 90 (2014).
[46] P. Torma, W.L. Barnes, Strong coupling between surface plasmon polaritons and emitters: a review, Rep. Prog. Phys. 78 (2015), 013901.
[47] J.P. Reithmaier, G. Sek, A. Loffler, C. Hofmann, S. Kuhn, S. Reitzenstein, L. V. Keldysh, V.D. Kulakovskii, T.L. Reinecke, A. Forchel, Strong coupling in a single quantum dot-semiconductor microcavity system, Nature 432 (2004) 197–200.
[48] H. Li, B. Chen, M. Qin, L. Wang, Strong plasmon-exciton coupling in MIM waveguide-resonator systems with WS_2 monolayer, Opt. Exp. 28 (2020) 205–215.
[49] H. Li, M. Qin, Y. Ren, J. Hu, Angle-independent strong coupling between plasmonic magnetic resonances and excitons in monolayer WS_2, Opt. Exp. 27 (2019) 22951–22959.

[50] E. Xifre-Perez, L. Shi, U. Tuzer, R. Fenollosa, F. Ramiro-Manzano, R. Quidant, F. Meseguer, Mirror-image-induced magnetic modes, ACS Nano 7 (2013) 664–668.
[51] Y.L. Kuo, S.Y. Chuang, S.Y. Chen, K.P. Chen, Enhancing the Interaction between High-Refractive Index Nanoparticles and Gold Film Substrates Based on Oblique Incidence Excitation, ACS Omega 1 (2016) 613–619.
[52] A.E. Miroshnichenko, A.B. Evlyukhin, Y.S. Kivshar, B.N. Chichkov, Substrate-Induced Resonant Magnetoelectric Effects for Dielectric Nanoparticles, ACS Photonics 2 (2015) 1423–1428.
[53] I. Sinev, I. Iorsh, A. Bogdanov, D. Permyakov, F. Komissarenko, I. Mukhin, A. Samusev, V. Valuckas, A.I. Kuznetsov, B.S. Luk'yanchuk, A.E. Miroshnichenko, Y.S. Kivshar, Polarization control over electric and magnetic dipole resonances of dielectric nanoparticles on metallic films, Laser Photonics Rev. 10 (2016) 799–806.
[54] H.R. Gutierrez, N. Perea-Lopez, A.L. Elias, A. Berkdemir, B. Wang, R. Lv, F. Lopez-Urias, V.H. Crespi, H. Terrones, M. Terrones, Extraordinary room-temperature photoluminescence in triangular WS_2 monolayers, Nano Lett. 13 (2013) 3447–3454.